https://ntrs.nasa.gov/search.jsp?R=20190026622 2019-09-26T19:30:26+00:00Z

Laser pulse bidirectional reflectance from CALIPSO mission

Xiaomei lu [1,2], Yongxiang Hu [2], Yuekui Yang [3], Mark Vaughan [2], Zhaoyan Liu [2], Sharon Rodier [1,2], Bill Hunt [1,2], Patricia Lucker [1,2], Charles Trepte [2]

[1] Science Systems and Applications, Inc., Hampton, VA, 23666, USA
[2] NASA Langley Research Center, Hampton, VA, 23681, USA
[3] NASA Goddard Space Flight Center, Greenbelt, MD, USA

Correspondence to: Xiaomei Lu (xiaomei.lu@nasa.gov); Yongxiang Hu (yongxiang.hu-1@nasa.gov)

Abstract. This paper presents an innovative retrieval method that translate the CALIOP land surface laser pulse returns into the surface bidirectional reflectance. To better analyze the surface returns, the CALIOP receiver impulse response and the downlinked samples' distribution at 30 m resolution are discussed. The saturated laser pulse returns from snow and ice surfaces are recovered based on surface tail information. The retrieved snow surface bidirectional reflectance is compared with reflectance from both CALIOP cloud cover regions and MODIS BRDF/Albedo model parameters. Besides the surface bidirectional reflectance, the column top-of-atmosphere bidirectional reflectance is calculated from the CALIOP lidar background data. It is compared with bidirectional reflectance from WFC radiance measurements. The retrieved CALIOP surface bidirectional reflectance and column top-of-atmosphere bidirectional reflectance results provide unique information to complement existing MODIS standard data products and would have valuable applications for modellers.

1 Introduction

The surface reflectivity over the snow and ice covered polar regions is a crucial factor in the Earth's radiation budget (Wiscombe and Warren, 1980). Although passive sensors, such as the Moderate-resolution Imaging Spectroradiometer (MODIS) instruments, which are operating on both Terra and Aqua spacecraft (Savtchenko et al., 2003), are being used by scientists from a variety of disciplines, including oceanography (McClain, 2009; NASA Goddard Space Flight Center, 2014a; NASA Goddard Space Flight Center, 2014b), biology (NASA Goddard Space Flight Center, 2014c) and atmospheric science (Platnick et al. 2015), their reflectance observations are limited to daylight seasons and have large uncertainties due to the low solar angles in the polar regions (Behrenfeld et al., 2013; Lu et al., 2017). In this regard, active sensors can complement passive sensors and provide new opportunities (Yang et al., 2013).

The Cloud-Aerosol Lidar and Infrared Pathfinder Satellite Observations (CALIPSO) mission builds on the experience of LITE, which flew a three-wavelength lidar on the Space Shuttle in 1994 (Hunt et al., 2009; Winker et al., 1996). The CALIPSO instrument suite consists of the Cloud-Aerosol Lidar with Orthogonal Polarization (CALIOP) a two-wavelength (1064 nm, 532 nm) polarization sensitive lidar, the Infrared Imaging Radiometer (IIR) that has three channels in the thermal infrared, and the Wide Field Camera (WFC) with a single channel at 650 nm. Additional details can be found in the

CALPSO algorithm theoretical basis documents (ATBDs) which are available online at (https://www-calipso.larc.nasa.gov/resources/project_documentation.php). Since science operations began on 7 June 2006, data have been collected almost continuously and all instruments have performed exceptionally well. CALIOP lidar provides vertical profiles of the elastic backscattering from a near nadir-viewing during both day and night between 82ºN and 82ºS (Hunt et al., 2009; Winker et al., 2009). Though largely ignored prior to launch, the signals from CALIOP surface returns have since been mined for a wealth of unanticipated new discoveries (Behrenfeld et al., 2017; He et al., 2016; Lu et al., 2016; Venkata and Reagan, 2016). These valuable signals can provide a wealth of unique information to complement existing A-Train Terra and Aqua MODIS passive remote sensing data products, including nighttime measurements, measurements underneath aerosols and non-opaque clouds, measurements in polar regions during all seasons and over sea-ice, and direct measurements of depolarization ratio at 532 nm.

In this study, we focus on the retrieval of surface laser pulse bidirectional reflectance, using the CALIOP 532 nm polarization channels. The method overview and initial assessment of the method performance will be presented. To better analyze the surface returns, the CALIOP receiver impulse response and the downlinked samples' distribution at 30 m resolution are discussed. The remainder of the paper is organized as follows: the CALIPSO, MODIS and Ice, Cloud and land Elevation Satellite (ICESat) data are briefly introduced in the next section; the surface bidirectional reflectance retrieval method and initial assessment are described in section 3; section 4 consists of the column bidirectional reflectance retrieval method and results; the final section outlines the conclusions of our analysis.

2 Data products

In this section, we provide the data products that are used in this paper. These include the CALIOP version 4 data, CALIPSO WFC data, MODIS bidirectional reflectance distribution function (BRDF) and Albedo products, and ICESat Geoscience Laser Altimetry System (GLAS) surface elevation data.

2.1 CALIPSO data

CALIOP version 4 level 1 data product are used here to derive the integrated attenuated backscatter that is a major parameter used in the surface bidirectional reflectance retrieval described in Section 3. Compared with version 3 data, the CALIOP version 4 data product substantially improves both the 532 nm and 1064 nm calibration accuracies. Changes to the calibration techniques were firmly rooted by a thoroughly documented and peer-reviewed approach (Getzewich et al., 2016; Liu et al., 2016). The product is available beginning with data from June 13, 2006 through now. Remaining data will be available as it is produced. More information about the data products including data availability, user documentation, quality statements, sample read software, and tools for working with the data, etc. can be found at the Atmospheric Science Data Center (ASDC) links (https://eosweb.larc.nasa.gov/project/calipso/calipso_table).

To obtain the surface laser pulse reflectance under clear skies, the integrated attenuated backscatter (IAB) above the surface is used to filter out signals with any significant atmospheric attenuation. The typical clear atmosphere is considered to be the case with IAB less than 0.0125 sr^{-1} (Venkata and Reagan, 2016). The CALIOP level 2 data product provides the cloud/aerosol optical properties, such as optical depth, cloud/aerosol layer base and top altitude, etc.

The WFC is a commercial-off-the-shelf instrument based on the Ball Aerospace & Technologies Corporation CT-633 star tracker design. The IFOV of each pixel in the camera is approximately 125 m by 125 m when projected onto the Earth's surface from a nominal 705 km orbit. The image plane is oriented such that the active row of pixels is aligned in the cross-track direction providing a full swath FOV of approximately 61 km in the cross-track direction centered on the lidar boresight. The WFC is designed to have a large dynamic range that will allow it to observe bright clouds without saturation and still be able to detect small variations in surface albedo (Pitts et al., 2005). The bi-directional reflectance from CALPSO WFC radiance measurements is archived in WFC level 1 data. The CALIOP level 1, level 2 and WFC level 1 data products can be freely downloaded through the ASDC at NASA Langley Research Center (https://eosweb.larc.nasa.gov/HORDERBIN/HTML_Start.cgi).

2.2 MODIS BRDF/Albedo Parameters

MODIS is an optical scanner that measures Earth radiance in 36 bands, ranging from 0.4 to 14 μm. The MODIS land surface reflectance is a seven-band product computed from the MODIS Level 1B land bands 1 (620-670 nm), 2 (841-876 nm), 3 (459-479 nm), 4 (545-565 nm), 5 (1230-1250 nm), 6 (1628-1652 nm) and 7 (2105-2155). The product provides an estimate of the surface spectral reflectance for each band as it would have been measured at ground level as if there were no atmospheric scattering or absorption. It corrects for the atmospheric gases' and aerosols' effects (Vermote, 2015a; Vermote, 2015b). In order to get surface reflectance with near nadir illumination and nadir viewing angles, the MODIS MCD43C1 version 6 bidirectional reflectance distribution function (BRDF) and Albedo parameters are used. The BRDF describes how the reflectance depends on view and solar angles. Specification of the BRDF provides land surface reflectance explicitly in terms of its spectral, directional, spatial, and temporal characteristics (Lucht et al., 2000). The operational MODIS BRDF/Albedo algorithm makes use of a kernel-driven, linear BRDF model which relies on the weighted sum of an isotropic parameter and two functions (or kernels) of viewing and illumination geometry to determine reflectance as: (Schaaf et al., 2002)

$$R(\theta, \upsilon, \phi, \lambda) = f_{iso}(\lambda) + f_{vol}(\lambda)K_{vol}(\theta, \upsilon, \phi, \lambda) + f_{geo}(\lambda)K_{geo}(\theta, \upsilon, \phi, \lambda) \quad (1)$$

where θ, υ, ϕ, λ are the solar zenith, view zenith, relative azimuth angles and wavelength, respectively. $K_k(\theta, \upsilon, \phi, \lambda)$ are the model kernels and $f_k(\lambda)$ are the spectrally dependent BRDF kernel parameters. The MODIS surface reflectance used in Section 3 is calculated by Eq. (1) with $f_k(\lambda)$ from MODIS MCD43C1 provided BRDF/Albedo parameters at band 4, and the model kernels $K_k(\theta, \upsilon, \phi, \lambda)$ by Eq. (38) and (39) of (Lucht et al., 2000) with 3° solar zenith and view zenith angle and 0°

relative azimuth angle. The MODIS MCD43C1 products are publically available and can be downloaded from NASA's Land Processes Distributed Active Archive Center (LP DAAC).

2.3 ICESat/GLAS surface elevation

NASA Ice, Cloud and land Elevation Satellite (ICESat), which operated between 2003 and 2009, made the first satellite-based global lidar measurement of Earth's ice sheet elevations, sea-ice thickness, and vegetation canopy structure. The primary instrument on ICESat was the Geoscience Laser Altimetry System (GLAS), which utilizes 1064 nm laser pulses for measuring the heights of the surface and samples the Earth's surface from an orbit of about 600 km with laser footprints of about 65 m in diameter spaced at 172 m along track. The primary objective of the GLAS laser altimeter is to measure elevation profiles of the Greenland and Antarctic ice sheet surfaces (Zwally et al., 2002). The GLAS/ICESat 500 m laser altimetry Digital Elevation Model (DEM) product of Antarctic (DiMarzio, 2007) were used in this paper. This DEM is generated from the first seven operational periods (from February 2003 through June 2005) of the GLAS instrument. It is provided on polar stereographic grids at 500 m grid spacing. The grid covers all of Antarctica north of 86° S.

3 CALIOP laser pulse bi-directional reflectance

In this section, we introduce the surface laser pulse bi-directional reflectance retrieval method. First, we give an introduction of the CALIOP receiver impulse response that is important for analyzing the surface signals. Then the saturated signal from snow and ice surfaces is recovered based on the surface tail information. Finally, the CALIOP surface laser pulse bi-directional reflectance results are validated.

3.1 Method

For CALIOP receiver at 532 nm, the Photomultiplier tubes (PMTs) are used for the detectors followed by a third-order low-pass Bessel filter with a bandwidth ~ 2.44 MHz (Venkata and Reagan, 2016). The output of the low-pass filter is sampled by the 10 MHz analog-to-digital converter (ADC), which is equivalent to the initial 15 m vertical resolution. To conserve bandwidth, the data acquired between 0.5 km below and 8.3 km above mean sea level are subsequently averaged on board the satellite to 30 m vertical resolution. A feature of the low-pass Bessel filter is that for a short pulse return (as occurs from a hard-target reflection) the area under the pulse is preserved. Figure 1(a) illustrates simulated example where the black curve is the hard surface return, the blue curve is the impulse response of the low-pass filter and the red curve is the convolution results between the black and blue curves. The surface elevation is assumed to be zero meter. The elevation below the surface is set to negative value. It can be seen from Figure 1(a) that if a narrow pulse (black) enters the low-pass filter, its peak amplitude is reduced but the pulse is stretched in time (or range r=ct/2, c the light speed, t travelling time) so as to preserve the area under the original narrow pulse. The shape of the post filter response is the CALIOP impulse response function, which is the convolution result between the original narrow pulse and impulse response of low-pass filter. Because

the width of the filter impulse response is much larger than the surface pulse as shown in Figure 1(a), the shape of CALIOP impulse response function is dominated by the filter impulse response and is relatively less sensitive to the pulse width of the transmitted laser pulse (20 ns width). Note that the blue curve and the red curve of Figure 1(a) are overlapping each other. Figure 1(b) shows the CALIOP impulse response model for the hard surface (blue curve) ((Hu et al., 2007) and simulated peak normalized surface pulse (black). Since the original narrow surface pulse of Figure 1(a) is stretched to the red line, the low pass filter can distribute a narrow surface return (black line) to a sequence of downlinked 30 m resolution samples (red circles) over several adjacent range bins starting from the bin that contains the surface echo. Please note that the downlinked samples in Figure 1(b) are supposed to have no time delay (Venkata and Reagan, 2016), that is, the digitized samples by the ADC is exactly coincident with the surface return pulse. However, on board CALIOP the start sampling time of ADC is variable. Different digitized samples can be obtained when ADC sampled and quantized the surface return pulse at different time. Figure 2 shows examples of downlinked samples at different ADC sampling times. The surface altitude ($z_{surface}$) is assumed to be zero meter (red dash line). The black and green dash lines are elevations where the downlinked surface sample is peak (z_{peak}). The elevation of downlinked surface peak of Figure 2(a) is lower than the true surface elevation and simultaneously the magnitude of samples immediately before the peak is increased and the magnitude of samples immediately after the peak is reduced. When the elevation of downlinked surface peak is higher than the surface elevation, the corresponding changes for the downlinked samples immediately before and after the peak are reversed (Figure 2(b)). Figure 2 indicates that the shape of the downlinked samples' distribution is determined by the distance between actual surface elevation and the elevation of downlinked surface peak ($z_{surface}$-z_{peak}) (Lu et al., 2014).

The observations show that the CALIOP impulse response exhibits the non-ideal recovery of the lidar signal after a strong backscattering target. Examples of strong targets are water clouds and surface returns (Hu et al., 2007; Lu et al., 2014). As a result, the surface total integrated attenuated backscatter (unit: sr^{-1}) is calculated as integrating between 30 meters above and 300 meters below the surface,

$$\gamma'_{total} = \int_{surface-300m}^{surface+30m} \beta'(z)dz \quad (2)$$

with the surface attenuated backscatter coefficients, $\beta'(z)$, obtained directly from CALIOP level 1 version 4 data product. The surface is determined to be the maximum attenuated backscatter located within 150 meters above or below the reported Global 30 arc-second (GTOPO30) Digital Elevation Model (https://lta.cr.usgs.gov/GTOPO30). Because of the non-ideal recovery of transient impulse response, the downlinked samples of Figure 1(b) wrongly appear as if the laser pulse is penetrating the surface to a depth of several hundreds of meters. It has been found that more than 90% of the surface return energy comes from the first three downlinked samples corresponding to that of the peak sample as well as one before and one after the peak sample as shown in Figure 1(b) and 2. Others of the surface return energy will spread into the tails (Hu et al. 2007). The integrated attenuated backscatter (unit: sr^{-1}) of surface tail is calculated as,

$$\gamma'_{tail} = \int_{surface-300m}^{surface-60m} \beta'(z)dz \quad (3)$$

The CALIOP observed integrated attenuated backscatter from land surface is the product of the actual surface bidirectional reflectance and atmospheric effective transmission (Josset et al., 2010): $\gamma'_{total} = \rho T^2/\pi$. The land surface bi-directional reflectance (ρ) can be obtained directly from the surface total integrated attenuated backscatter as,

$$\rho = \gamma'_{total}\pi/T^2 \quad (4)$$

T^2 is the two-way atmospheric transmittance which can be estimated from the CALIOP data (Hu et al., 2008). The ocean surface reflectance from CALIOP lidar measurements can be found in detail from reference (Venkata and Reagan, 2016). For the clear sky, the molecular Rayleigh two-way atmospheric transmittance can be estimated directly from Rayleigh extinction cross-section and molecular number density reported for each lidar profile from the ancillary meteorological data provided by the NASA Global Modeling and Assimilation Office (GMAO) (https://gmao.gsfc.nasa.gov/operations/). For cloudy (or aerosol) skies, the cloud (or aerosol) optical depth can be found from CALIOP level 2 cloud (or aerosol) layer or profile products. However, the signals from snow and ice surfaces under clear skies are so strong that they usually saturate the digitizers. For the saturated signal, we should recover the saturated signal first before calculating the surface bi-directional reflectance from Eq. (4).

3.2 recovery of CALIOP Saturated signal

Two 14-bit ADCs with different gains are used in each 532-nm channel to provide the required 22-bit effective dynamic range. On each channel, the high gain ADC measures weak signals and the low gain ADC acquires signals which saturate the high gain digitizer. The profile samples are taken from the high-gain ADC if they are on-scale. If a sample is saturated on the high-gain ADC, the corresponding sample from the low-gain ADC, rescaled by the gain ratio between the high gain channel and the low gain channel (High-Low gain ratio), is used. The output of each pair of digitizers are re-scaled and merged into a single profile before being downlinked. The downlinked signal is saturated when the low gain channel signal is saturated. The value that gets rescaled is the backscatter signal from the low gain channel, which is the total signal minus the offset. The maximum digitizer reading is 16383 (14 bits). Thus, the maximum backscatter value when the low gain channel reaches saturation is 16383-offset. The corresponding saturation value is the maximum low gain channel backscatter (16383-offset) multiplied by the High-Low gain ratio. Moreover, because multiple samples are averaged before downlinking, it is possible that a downlinked sample value might be less than the saturation value, and yet one of the samples that went into the average might be saturated. Please note that the saturation value here is different from the value reported in CALPSO level 1 data product. To apply the saturation calculation to level 1 data, some additional conversions (e.g., range-scaled, energy normalized, calibration and amplifier gain normalized, etc.) are required.

For users' convenient, surface saturation flag used to indicate the likelihood that the surface backscatter signal is saturated has been added to the CALIOP version 4 level 1 data product. The surface saturation flag values of 0, 1 and 2 mean the surface backscatter signal is not saturated, possibly saturated and certainly saturated, respectively. In order to see the saturated and not saturated surface backscatter signal, Figure 3 and 4 show the relation between total and tail surface integrated attenuated backscatter at CALIOP 532 nm parallel and perpendicular channels, respectively. The color is the

number of CALIOP lidar observations. Figure 3(a) is for the total surface observations, 3(b) is for surface observations that are not saturated, 3(c) is for the observations that are possibly saturated and 3(d) is for the certainly saturated surface observations. The green and black lines are the simulated total-to-tail signal ratios for not saturated and saturated surface backscatter signals from the CALIOP impulse response model shown in Figure 1(b) where the saturation value is set to be 1.4 $km^{-1}sr^{-1}$ and the simulated downlinked samples have no time delay. The green and black lines are overlap when the surface returns are small and not saturated. However, the black line distorted from green line when the surface returns are saturated. Figure 4 is the same as Figure 3 but for the CALIOP 532 nm perpendicular channel. Figure 3 and 4 show that there is linear relation between total and tail surface integrated attenuated backscatter (green line) for not-saturated surface backscatter signals. For the saturated signals, the total integrated attenuated backscatter (γ'_{total}) can be estimated from the surface tail γ'_{tail} as:

$$\gamma'_{total} = c\gamma'_{tail} \quad (5)$$

The value of c is the total-to-tail signal ratio which can be estimated from fitting the total and tail signals of not saturated CALIOP observations shown in Figure 3(b) and 4(b), and it can be theoretically obtained from the CALIOP impulse response model shown in Figure 1(b) as well. The value of c is about 19.6 from fitting the not saturated signal. Since the shape of the downlinked samples' distribution is determined by the distance between actual surface elevation and the elevation of downlinked surface peak ($z_{surface}$-z_{peak}), the value of total-to-tail signal ratio is also a function of the distance $z_{surface}$-z_{peak} as shown in Figure 5, which is estimated from the impulse response model of Figure 1(b) by setting different ADC sampling times corresponding to the distance $z_{surface}$-z_{peak} from about -15 m to 15 m. The advantage of using surface tail to estimate the total integrated attenuated backscatter (Eq. 5) is that the surface tail will not be subject to saturation.

3.3 Validation

The surface return from snow and ice would saturate the detectors under clear sky or thin cloud situations. Figure 6 shows CALIOP data image of 532 nm total attenuated backscatter (km^{-1} sr^{-1}) on October 10th 2009 over Antarctic snow surface. The color bar on the right stands for the value of total attenuated backscatter at 532 nm. The surface return under clear sky within the red dash lines are certainly saturated, while the surface return signals between the green dash lines under transparent cloud are not saturated. The surface signals between red and green dash lines under transparent cloud are possibly saturated. The 532 nm non-ideal transient recovery is seen in the Figure 6 image as a gradual transition of colors from high attenuated backscatter values (white) to lower ones for the snow surface under clear sky (between red dash lines). The CALIOP ground-track orbit is shown as black line in Figure 7, where the green orbits are corresponding to the not-saturated region and red orbits are corresponding to the saturated region of Figure 6. The background color is the snow surface elevation (unit meter) from GLAS/ICESat 500 m laser altimetry Digital Elevation Model (DEM) product of Antarctica (DiMarzio, 2007).

For the saturated region of Figure 6, the total integrated attenuated backscatter (γ'_{total}) of snow surface is calculated from surface tail by Eq. (5) with the total-to-tail signal ratio obtained from Figure 5. The required elevation difference ($z_{surface}$-

z_{peak}) is between GLAS/ICESat Antarctica DEM and CALIOP downlinked surface peak. Here the GLAS/ICESat Antarctica DEM is supposed to be the true surface elevation. The surface bi-directional reflectance (ρ) is then obtained from Eq. (4) with the clear sky two-way atmospheric transmittance derived from meteorological data reported in the CALIOP level 1 profiles. The surface bi-directional reflectance estimated from the surface tail is presented in red of Figure 8(a). For comparison, the CALIOP observed surface bi-directional reflectance with the total integrated attenuated backscatter (γ'_{total}) calculated by Eq.(2) directly from saturated surface return is shown in blue. For the not-saturated region of Figure 6, the cloud optical depth (τ_c) is from the corresponding CALIOP level 2 cloud layer data products. The cloud two-way transmittance is estimated as: $\exp(-2\tau_c)(1+\tau_c/2)^2$ (Yang et al., 2013). The CALIOP observed surface reflectance before and after correcting the cloud transmittance are shown in blue and red in Figure 8(b), respectively. Figure 8 indicates that the surface reflectance directly from the saturated signals (blue in Figure 8(a)) will be lower than its true values. Moreover, when clouds are present the surface reflectance before correcting the cloud transmittance (0.18±0.04) is much smaller than the ones from the saturated signal under clear sky conditions (0.58±0.02). The mean surface reflectance estimated from the surface tail over the saturated region is about 0.86±0.06 while the mean surface reflectance by correcting the cloud transmittance from not-saturated region is about 0.89±0.07. The mean surface reflectance estimated from the surface tail is consistent with the reflectance after correcting the cloud transmittance.

Figure 9 presents more CALIOP surface reflectance comparisons over Antarctica for clear sky (solid curves) and cloudy sky (dash curves) conditions in 2009. The solid black is reflectance distribution estimated from surface tail with the constant total-to-tail signal ratio of 19.6 used in Eq. (5), while the solid red is reflectance directly obtained from the saturated signals by Eq. (2) and (4). The dash red and black are surface reflectance before and after correcting the cloud transmittance. The clouds are chosen with the optical depth of about 1 to make sure that the surface return under cloud is not saturated and as well as it is not too small to have lower signal to noise ratio. When clouds are present, the mean surface reflectance before correcting the cloud transmittance (red dash curve) is about 0.26±0.05. The mean surface reflectance from saturated signal is about 0.58±0.05. The red dash is totally separated from solid red distribution which indicates that the surface reflectance at 532 nm over polar snow/ice sheet regions could be used as cloud screening when cloud optical depth is greater than 1. The mean surface reflectance estimated from the surface tail (solid black) is about 0.90±0.10 while the mean surface reflectance by correcting the cloud transmittance (dash black) from cloud region is about 0.84±0.13. Please note that only first scattering order is taken into account when calculating cloud two-way transmittance. The surface reflectance under cloud conditions will be more accurate if the cloud two-way transmittance can be obtained more accurately. The pink is MODIS reflectance distribution at 555 nm with the mean of about 0.96±0.04. The surface bidirectional reflectance results shown in Figure 9 are from one-year of CALIOP observations over Antarctica. The surface reflectance might be variable due to snow aging, dust or soot content, melting and surface roughness etc. As a consequence, the standard deviation of surface reflectance reported here is larger than the simulated one of about 0.004 (Yang et al., 2013). For example, we assume here a 5% uncertainty of surface tail γ'_{tail} and two-way atmospheric transmittance T^2, 10% uncertainty of the total-to-tail signal ratio c. From Eqs. (5)

and (4), the uncertainty of surface bi-directional reflectance can be estimated as $\frac{\Delta^2\rho}{\rho^2} = \frac{\Delta^2\gamma'_{tail}}{\gamma'^2_{tail}} + \frac{\Delta^2 c}{C^2} + \frac{4\Delta^2 T^2}{T^2}$. Summing up all the uncertainties yields the value of $\frac{\Delta^2\rho}{\rho^2}$ as 0.02, resulting the uncertainty in surface bi-directional reflectance ($\frac{\Delta\rho}{\rho}$) is about 14%. The standard deviation will be about 0.13 with the mean value of surface bi-directional reflectance of about 0.9. The retrieved CALIOP surface bidirectional reflectance from surface tail is consistent with reflectance for snow samples with melting and refreezing cycle (Wiscombe and Warren, 1980), and agrees with reflectance for snow samples in presence of volcanic sand and soot (Peltoniemi et al., 2015).

Figure 10 shows the monthly CALIOP surface reflectance at 532 nm for clear sky condition in 2009. The color bar stands for the value of surface reflectance. The surface reflectance for the saturated observations are obtained from the surface tail with the constant total-to-tail signal ratio of 19.6, while the surface reflectance for not-saturated observations are estimated directly from Eq. (2) and (4). The monthly surface reflectance shows that the reflectance values over permanent snow and ice surfaces (Greenland and Antarctica) are high during the whole year, and the reflectance results over snow covered land surface in winter time are higher than those in summer time when the snow are completely melted. There is significant seasonal reflectance transition from winter (December, January and February), to spring (March, April and May), to summer (June, July and August) and then to Fall (September, October and November). The pattern of CALIOP surface reflectance at 532 nm is similar to that of MODIS surface reflectance at 555 nm presented in Figure 11, which is calculated from MODIS provided BRDF/Albedo parameters with 3° off nadir illumination angles. We note that there are no MODIS results at high latitude during polar night. This new surface reflectance records from CALIOP lidar, which is insensitive to lighting conditions and has an ability to characterize the surface even when obscured by transparent cloud, complement existing MODIS passive remote sensing capabilities.

4 CALIOP Column bi-directional reflectance

Beside the surface bidirectional reflectance, an effort is underway to use the CALIOP lidar background data to compute the column top-of-atmosphere bi-directional reflectance, as defined by the following equation:

$$\rho = \frac{\pi I}{\mu_0 S_0 D} \quad (6)$$

where μ_0 is cosine of the solar zenith angle. I is the upwelling radiance derived from the lidar background signals. The upwelling radiance is proportional to the lidar background, which is proportional to the square of the root man square (RMS) noise. S_0 is the extraterrestrial solar irradiance over the lidar bandpass. D is an adjustment for the correct Earth-Sun distance (Spencer, 1971). The upwelling background radiance, I, can be derived from either the background monitor anode current readings or the RMS baseline noise. The background monitor readings may be subject to uncertainty in offsets and also the possibility of saturation over bright targets. The square of the RMS baseline noise is highly correlated with the background monitor readings, but will not be subject to offset uncertainty or saturation. The RMS background noise is one of the

downlinked status parameters and will not have to be computed from science data. In terms of the RMS baseline noise, the parallel and perpendicular components of the upwelling background radiance can be expressed as $I_{\parallel} = C_{\parallel} RMS_{\parallel}^2, I_{\perp} = C_{\perp} RMS_{\perp}^2$, Where $RMS_{\parallel}$ and $RMS_{\perp}$ are the parallel and perpendicular components of the baseline noise and $C_{\parallel}$ and $C_{\perp}$ are the parallel and perpendicular calibration coefficients that relate the RMS noise values to radiance units. In addition, the calibration coefficients are related through the lidar polarization gain ratio (PGR) as $C_{\perp} = PGR \times C_{\parallel}$. The parallel and perpendicular components of the column reflectance can be expressed as,

$$\rho_{\parallel} = \frac{C_{\parallel} RMS_{\parallel}^2}{\mu_0 S_0 D} \quad (7)$$

$$\rho_{\perp} = \frac{PGR \times C_{\parallel} RMS_{\perp}^2}{\mu_0 S_0 D} \quad (8)$$

The total column reflectance is then the sum of parallel and perpendicular components. CALIOP version 4 level 1 data product provide the values of parallel and perpendicular column reflectance for single laser shot. Figure 12, 13 and 14 show examples of column reflectance from level 1 data on September 4th 2006. The blue line of Figure 12 is the CALIOP ground orbit track where the red one is region for the results shown in Figure 13 and 14. CALIOP data image of 532 nm total attenuated backscatter (km^{-1} sr^{-1}) is given in Figure 13, which shows the cloud and ocean surfaces. In Figure 14 we show the column reflectance values from both the CALIOP lidar (red) and the WFC (green) for the orbit shown in red line of Figure 12. The column reflectance values computed from the lidar data are consistent with the values from the camera. The relative differences are within 20%. The reason for the discrepancies could come from imperfect matching of the times of the WFC and the lidar observations, surface FOV differences and detector spectral response function differences. A global map of CALIOP column reflectance under clear sky condition for each month in 2009 is shown in Figure 15. The column reflectance is directly from CALIOP level 1 data and averaged over 1° by 2° latitude and longitude grid boxes. The column reflectance for Greenland and Antarctica are seen to be fairly consistent values in the range from 0.8 to about 1.1 with mean value of 0.94. The column reflectance over ocean surface varies between near zero to about 0.2. For the land surfaces, the column reflectance can be from 0.05 to about 0.4 with somewhat higher values in desert regions. Please note the column reflectance is available only on CALIOP daytime measurements since it is retrieved from the solar background signals. The CALIOP column bi-directional reflectance records can be used to model the solar background radiance in the lidar simulator tool (Powell et al., 2017).

5 Conclusion and Summary

In this paper, the laser pulse bidirectional reflectance is obtained from CALIOP surface returns, where the saturated pulse return from snow and ice surfaces was recovered from the surface tail. The snow surface bidirectional reflectance from surface tail was compared with MODIS surface reflectance and that from CALIOP not-saturated surface returns when cloud is present. The comparisons show that the snow surface bidirectional reflectance over Antarctica for saturation region are generally reliable with a mean value of about 0.90±0.10, while the mean surface reflectance from cloud cover region is about

0.84±0.13 and the calculated MODIS reflectance at 555 nm from BRDF/Albedo model with near nadir illumination and viewing angles is about 0.96±0.04. The comparisons here demonstrate that the snow surface reflectance underneath the cloud with cloud optical depth of about 1 is significant lower than that for clear sky condition. The surface reflectance results here support the cloud detection/screening in satellite data analysis. Moreover, CALIOP lidar makes reliable and independent measurements both day and night, and at low solar angles through considerable aerosol loads and transparent clouds. The surface bidirectional reflectance retrieved from CALIOP lidar measurements contribute complementary data for existing MODIS standard data products and could be used to detect and monitor seasonal surface reflectance changes in high latitude regions where passive MODIS measurements are limited.

The column top-of-atmosphere bidirectional reflectance from CALIOP version 4 data products is calculated from the square of the RMS baseline noise. The RMS baseline noise is highly correlated with the CALIOP background monitor readings and is not subject to offset uncertainty or saturation. The comparison analysis shows that the column reflectance values computed from the lidar data are consistent with the values from the WFC camera. For clear skies, the column bidirectional reflectance over Greenland and Antarctica is in the range from 0.8 to about 1.1 with mean value of 0.94, the column reflectance over ocean surface varies between near zero to about 0.2 and the column reflectance over land can be from 0.05 to about 0.4 with somewhat higher values in desert regions. These CALIOP column bi-directional reflectance records can be used to suggest the values of the solar background radiance required in the lidar simulator tools.

References

Behrenfeld, M. J., Hu, Y., Hostetler, C. A., Dall'Olmo, G., Rodier, S. D., Hair, J. W., and Trepte, C. R.: Space-based lidar measurements of global ocean carbon stocks, Geophys. Res. Lett., 40, 4355-4360, doi:10.1002/grl.50816, 2013.

Behrenfeld, M. J., Hu, Y., O/'Malley, R. T., Boss, E. S., Hostetler, C. A., Siegel, D. A., Sarmiento, J. L., Schulien, J., Hair, J. W., Lu, X., Rodier, S., and Scarino, A. J.: Annual boom-bust cycles of polar phytoplankton biomass revealed by space-based lidar, Nature Geosci., 10, 118-122, doi:10.1038/ngeo2861, 2017.

DiMarzio, J. P.: GLAS/ICESat 500 m Laser Altimetry Digital Elevation Model of Antarctica, Version 1, Boulder, Colorado USA. NSIDC: National Snow and Ice Data Center. doi: http://dx.doi.org/10.5067/K2IMI0L24BRJ.[10/24/2017 Accessed], 2007.

Getzewich, B. J., Tackett, J. L., Kar, J., Garnier, A., Vaughan, M. A., and Hunt, B.: CALIOP Calibration: Version 4.0 Algorithm Updates, EPJ Web of Conferences, 119, 04013, doi: https://doi.org/10.1051/epjconf/201611904013, 2016.

He, M., Hu, Y., Huang, J. P., and Stamnes, K.: Aerosol optical depth under 'clear' sky conditions derived from sea surface reflection of lidar signals, Opt. Exp., 24, A1618-A1634, doi:10.1364/OE.24.0A1618, 2016.

Hu, Y., Powell, K., Vaughan, M., Tepte, C., Weimer, C., Beherenfeld, M., Young, S., Winker, D., Hostetler, C., Hunt, W., Kuehn, R., Flittner, d., Cisewski, M., Gibson, G., Lin, B., and MacDonnell, D.: Elevation information in tail (EIT) technique for lidar altimetry, Opt. Express, 15, 14504-14515, doi:10.1364/OE.15.014504, 2007.

Hu, Y., Stamnes, K., Vaughan, M., Pelon, J., Weimer, C., Wu, D., Cisewski, M., Sun, W., Yang, P., Lin, B., Omar, A., Flittner, D., Hostetler, C., Trepte, C., Winker, D., Gibson, G., and Santa-Maria, M.: Sea surface wind speed estimation from space-based lidar measurements, Atmos. Chem. Phys., 8, 3593-3601, doi:10.5194/acp-8-3593-2008, 2008.

Hunt, W. H., Winker, D. M., Vaughan, M. A., Powell, K. A., Lucker, P. L., and Weimer, C.: CALIPSO Lidar Description and Performance Assessment, J. Atmos. Oceanic Technol., 26: 1214-1228, doi:10.1175/2009JTECHA1223.1, 2009.

Josset, D., Pelon, J., Hu, Y., Zhai, P., Powell, K., Rodier, S., and Trepte, C.: CALIPSO Land Surface Mapping Principle and First Results, 25th International Laser Radar Conference (ILRC), St. Petersburg, Russia, Curran Associates, Inc., 1316-1319, 2010.

Liu, Z., Winker, D., Omar, A., Vaughan, M., Kar, J., Trepte, C., Hu, Y., Schuster, G., and Young, S.: Aerosol Optical Properties Above Opaque Water Clouds Derived From The Caliop Version 4 Level 1 Data, EPJ Web of Conferences, 119, 04010, doi:https://doi.org/10.1051/epjconf/201611904010, 2016.

Lu, X., Hu, Y., C., T., and Liu, Z.: A Super-Resolution Laser Altimetry Concept, IEEE Geosci. Remote Sens. Lett., 11, 298-302, doi: 10.1109/lgrs.2013.2256876, 2014.

Lu, X., Hu, Y., Liu, Z., Rodier, S., Vaughan, M., Lucker, P., Trepte, C., and Pelon, J.: Observations of Arctic snow and sea ice cover from CALIOP lidar measurements, Remote Sens. Environ., 194, 248-263, doi: http://doi.org/10.1016/j.rse.2017.03.046., 2017.

Lu, X., Hu, Y., Pelon, J., Trepte, C., Liu, K., Rodier, S., Zeng, S., Lucker, P., Verhappen, R., Wilson, J., Audouy, C., Ferrier, C., Haouchine, S., Hunt, B., and Getzewich, B.: Retrieval of ocean subsurface particulate backscattering coefficient from space-borne CALIOP lidar measurements, Opt. Express, 24, 29001-29008, doi:10.1364/OE.24.029001, 2016.

Lucht, W., Schaaf, C. B., and Strahler, A. H.: An algorithm for the retrieval of albedo from space using semiempirical BRDF models, IEEE Trans. Geosci. Remote Sens., 38, 977-998, doi:10.1109/36.841980, 2000.

McClain, C. R.: A Decade of Satellite Ocean Color Observations, Annual Review of Marine Science, 1, 19-42, doi: 10.1146/annurev.marine.010908.163650, 2009.

NASA Goddard Space Flight Center, O. E. L., Ocean Biology Processing Group: Moderate-resolution Imaging Spectroradiometer (MODIS) Aqua Downwelling Diffuse Attenuation Coefficient Data, 2014 Reprocessing. NASA OB.DAAC, Greenbelt, MD, USA, doi: 10.5067/AQUA/MODIS/L3B/KD/2014, 2014a.

NASA Goddard Space Flight Center, O. E. L., Ocean Biology Processing Group: Moderate-resolution Imaging Spectroradiometer (MODIS) Aqua Remote-Sensing Reflectance Data, 2014 Reprocessing. NASA OB.DAAC, Greenbelt, MD, USA, doi: 10.5067/AQUA/MODIS/L3M/RRS/2014, 2014b.

NASA Goddard Space Flight Center, O. E. L., Ocean Biology Processing Group: Moderate-resolution Imaging Spectroradiometer (MODIS) Aqua Particulate Organic Carbon Data, 2014 Reprocessing NASA OB.DAAC, Greenbelt, MD, USA doi: 10.5067/AQUA/MODIS/L3B/POC/2014, 2014c.

Peltoniemi, J. I., Gritsevich, M., Hakala, T., Dagsson-Waldhauserová, P., Arnalds, Ó., Anttila, K., Hannula, H. R., Kivekäs, N., Lihavainen, H., Meinander, O., Svensson, J., Virkkula, A., and de Leeuw, G.: Soot on Snow experiment: bidirectional reflectance factor measurements of contaminated snow, The Cryosphere, 9, 2323-2337, doi: 10.5194/tc-9-2323-2015, 2015.

Pitts, M. C., Hu, Y., Currey, J. C., Winker, D., and Lambeth, J. D.: CALIPSO Algorithm Theoretical basis Document: Wide Field Camera (WFC) Level 1 Algorithms PC-SCI-205, doi: https://www-calipso.larc.nasa.gov/resources/project_documentation.php, 2005.

Platnick, S., Ackerman, S. A., King, M. D., Meyer, K., Menzel, W. P., Holz, R. E., Baum, B. A., and Yang, P.: MODIS atmosphere L2 cloud product (06_L2), NASA MODIS Adaptive Processing System, Goddard Space Flight Center, USA, 2015.

Powell, K. A., Hunt, W., Vaughan, M. A., Hair, J. W., and Hostetler, C. A.: Modeling Lidar Solar Background Measurements, The 97th AMS annual meeting: Session 4 The CALIPSO Mission: Space-based Atmospheric Studies -Part II, Seattle, WA, 2017.

Savtchenko, A., Ouzounov, D., Gopalan, A., Yuan, D., Nickless, D., and Ostrenga, D.: MODIS data from Terra and Aqua satellites, Geoscience and Remote Sensing Symposium, 2003. IGARSS '03. Proceedings. 2003 IEEE International, 5, 3028-3030, doi: 10.1109/IGARSS.2003.1294670, 2003.

Schaaf, C. B., Gao, F., Strahler, A. H., Lucht, W., Li, X., Tsang, T., Strugnell, N. C., Zhang, X., Jin, Y., Muller, J.-P., Lewis, P., Barnsley, M., Hobson, P., Disney, M., Roberts, G., Dunderdale, M., Doll, C., d'Entremont, R. P., Hu, B., Liang, S., Privette, J. L., and Roy, D.: First operational BRDF, albedo nadir reflectance products from MODIS, Remote Sens. Environ., 83, 135-148, doi: https://doi.org/10.1016/S0034-4257(02)00091-3, 2002.

Spencer, J. W.: Fourier Series Representation of the Position of the Sun, Search, Vol. 2, 172, 1971.

Venkata, S. and Reagan, J.: Aerosol Retrievals from CALIPSO Lidar Ocean Surface Returns, Remote Sens., 8, 1006, 2016a.

Vermote, E.: MOD09A1 MODIS Surface Reflectance 8-Day L3 Global 500m SIN Grid V006, NASA EOSDIS Land Processes DAAC, 2015a.

Vermote, E. F.: MODIS Surface Reflectance User's Guide, collection 6, Version 1.4, 2015b.

Winker, D. M., Couch, R. H., and McCormick, M. P.: An overview of LITE: NASA's Lidar In-space Technology Experiment, Proceedings of the IEEE, 84, 164-180, 1996.

Winker, D. M., Vaughan, M. A., Omar, A., Hu, Y., Powell, K. A., Liu, Z., Hunt, W. H., and Young, S. A.: Overview of the CALIPSO Mission and CALIOP Data Processing Algorithms, J. Atmos. Oceanic Technol., 26, 2310-2323, doi: 10.1175/2009jtecha1281.1, 2009.

Wiscombe, W. J. and Warren, S. G.: A Model for the Spectral Albedo of Snow. I: Pure Snow, J. Atmospheric Sci., 37, 2712-2733, doi: 10.1175/1520-0469(1980)037<2712:amftsa>2.0.co;2, 1980.

Yang, Y., Marshak, A., Palm, S. P., Wang, Z., and C. Schaaf: Assessment of Cloud Screening With Apparent Surface Reflectance in Support of the ICESat-2 Mission, IEEE Trans. Geosci. Remote Sens., 51, 1037-1045, doi: 10.1109/TGRS.2012.2204066, 2013.

Zwally, H. J., Schutz, B., Abdalati, W., Abshire, J., Bentley, C., Brenner, A., Bufton, J., Dezio, J., Hancock, D., Harding, D., Herring, T., Minster, B., Quinn, K., Palm, S., Spinhirne, J., and Thomas, R.: ICESat's laser measurements of polar ice, atmosphere, ocean, and land, J. Geodyn., 34, 405-445, 2002.

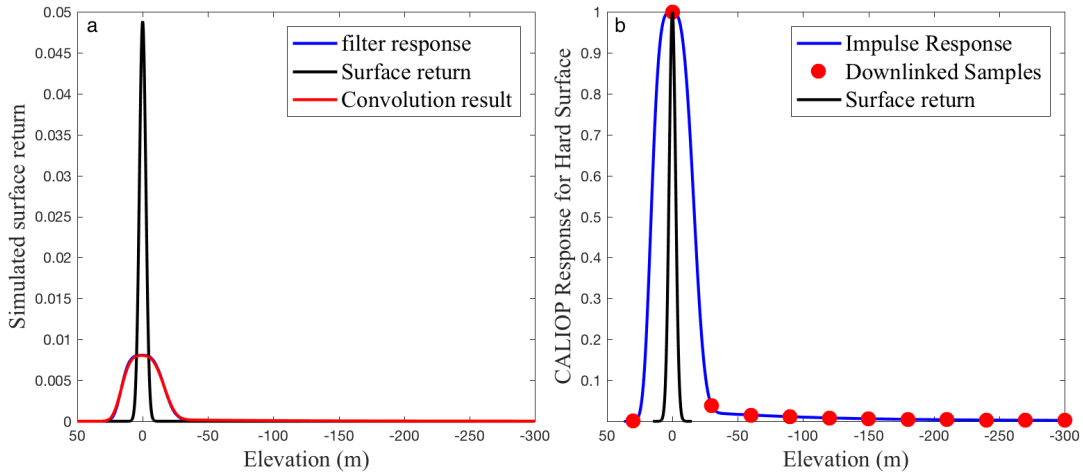

Figure 1 (a): simulated low-pass filter response (blue), surface return (black) and the convolution result of the surface return and low-pass filter (red). Note that the blue curve and the red curve are overlapping each other.; (b): CALIOP impulse response function for hard surface (blue) [32], the downlinked 30 m vertical resolution samples (red circles) and the simulated peak-normalized surface return (black). Note that the downlinked samples here are supposed to have no time delay [17]. The surface elevation is assumed to be 0 meter. The elevation below the surface is set to negative value.

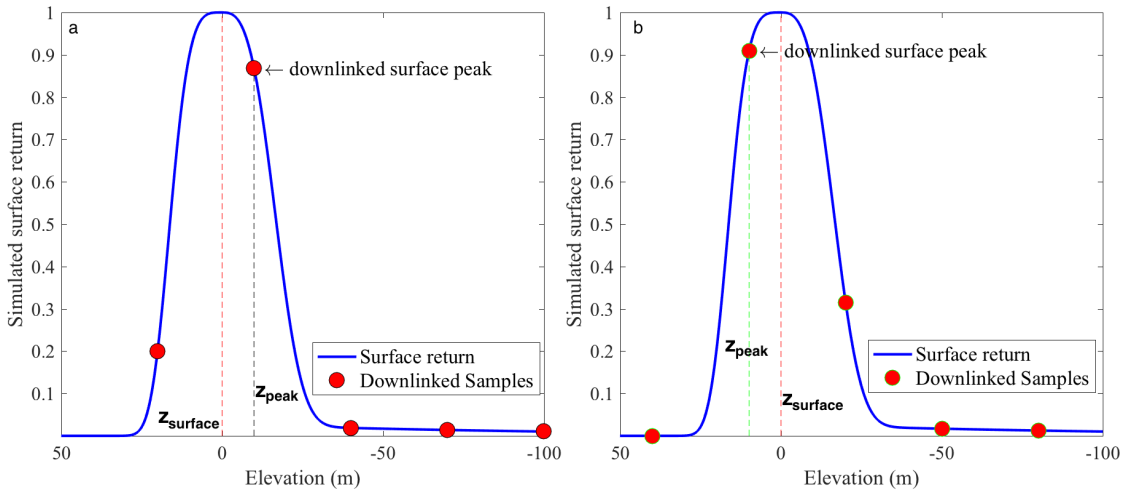

Figure 2 The simulated surface return pulse after low-pass filter (blue curve) and CALIOP downlinked 30 m resolution samples (red circles). The surface elevation (zsurface) is assumed to be 0 meter (red dash line). The elevation below the surface is set to negative value. The black and green dash lines are elevations where the downlinked surface sample is peak (zpeak).

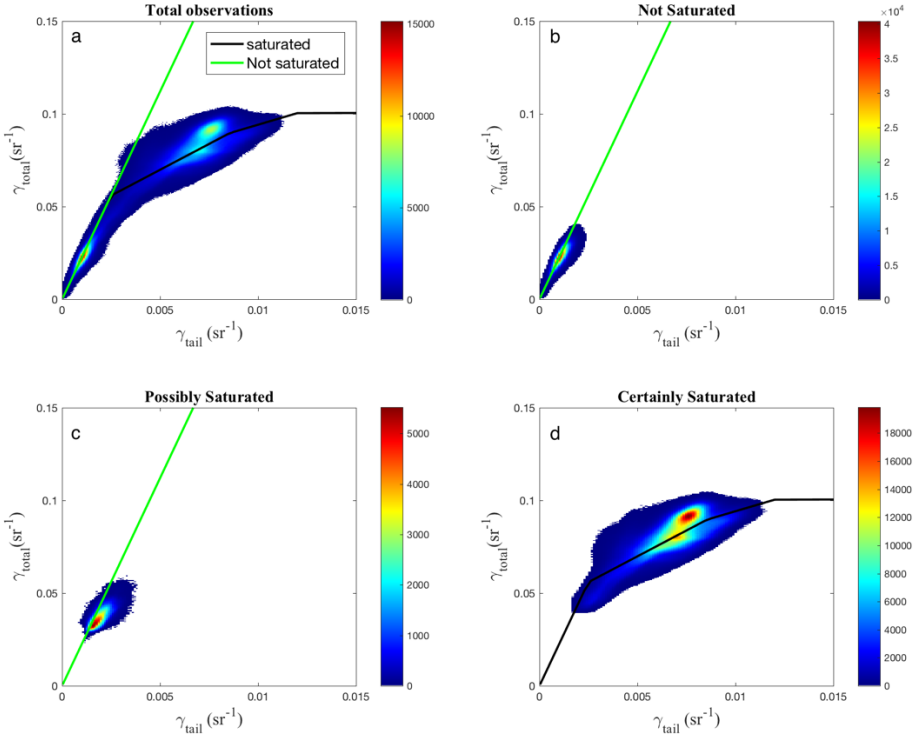

Figure 3. Relation between total γ'_{total} and tail γ'_{tail} integrated attenuated backscatter at CALIOP 532 nm parallel channel. (a) total observations; (b) not saturated observations; (c) possibly saturated observations; (d) certainly saturated observations. The color bar is the number of observations. The green and black lines are the simulated total-to-tail signal ratios for not saturated and saturated surface returns from the CALIOP impulse response function shown in Figure 1(b).

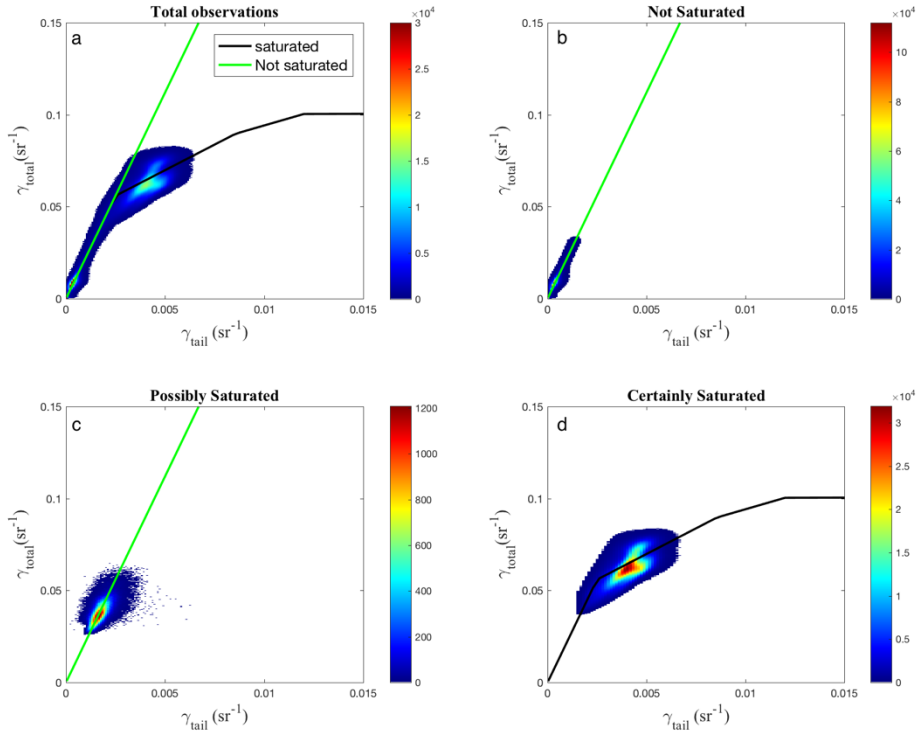

Figure 4. The same as Figure 3 but for the CALIOP 532 nm perpendicular channel.

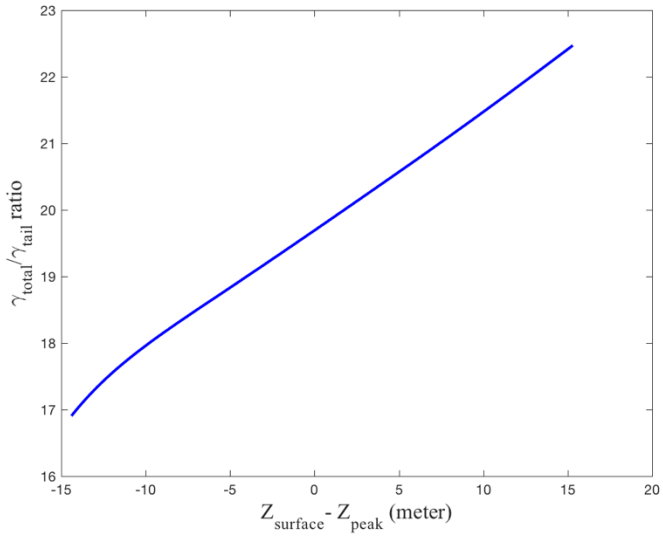

Figure 5 The total-to-tail signal ratio as a function of the elevation difference between actual surface and downlinked surface sample peak $z_{surface}$-z_{peak}.

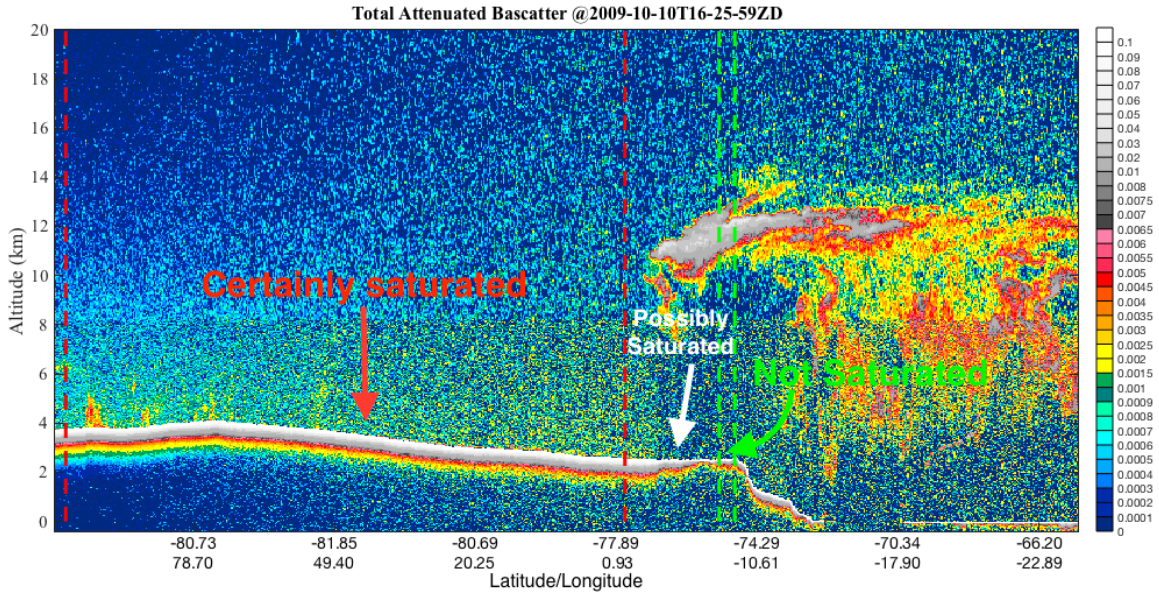

Figure 6. Total Attenuated backscatter at 532 nm (km-1 sr-1) on October 10th 2009; The surface return signals within the red dash lines under clear sky are certainly saturated, while the signals between the green dash lines under transparent cloud are not saturated. The surface signals between red and green dash lines under transparent cloud are possibly saturated. The color bar on the right stands for the value of total attenuated backscatter.

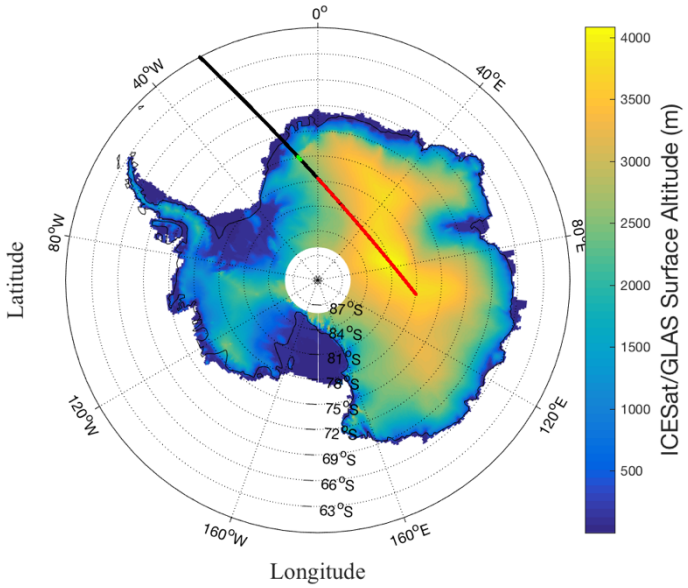

Figure 7 CALIOP ground-track over Antarctic (black line). Green orbits are corresponding to the not saturated region and red orbits are corresponding to the saturated region of Figure 6; The background color is the snow surface elevation (unit meter) from GLAS/ICESat Antarctic 500 m DEM product.

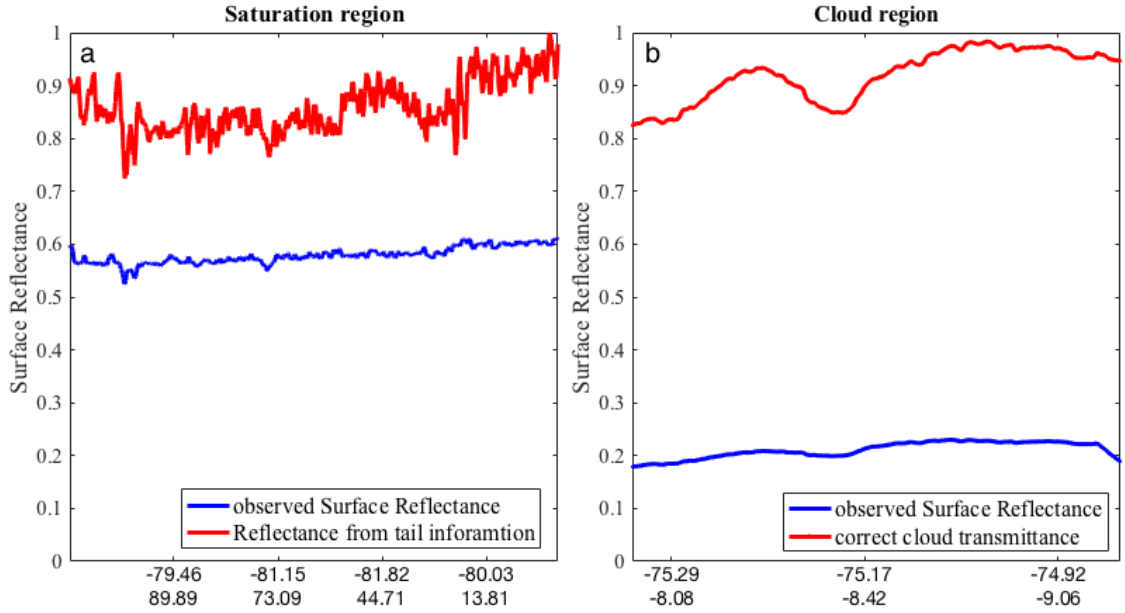

Figure 8. Left panel (a): CALIOP observed surface bidirectional reflectance (blue) and corrected surface bidirectional reflectance (red) corresponding to the saturated region of Fig. 6; Right panel (b): CALIOP observed surface bidirectional reflectance under transparent cloud before (blue) and after (red) correcting the cloud transmittance. It is corresponding to the not-saturated region of Fig. 6.

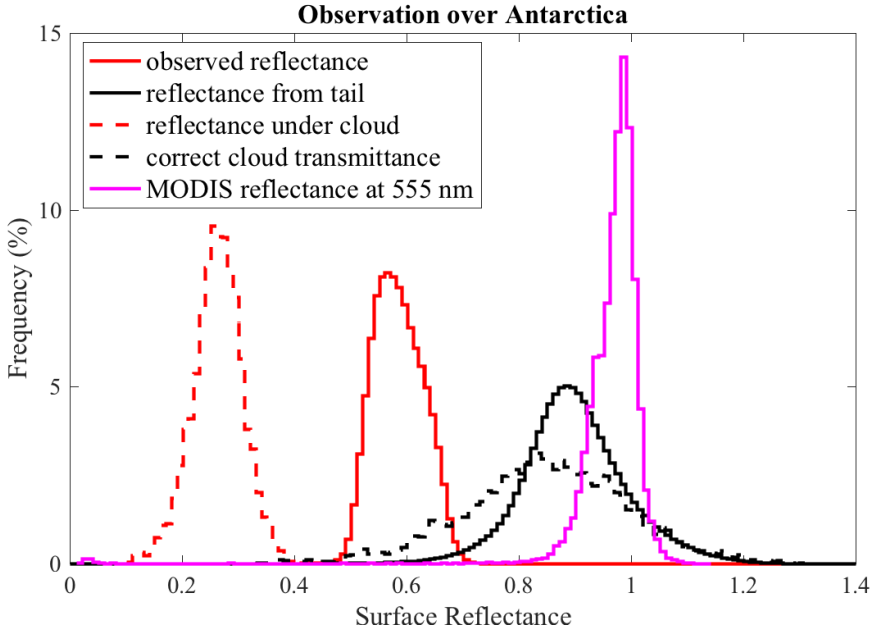

Figure 9 The CALIOP surface bidirectional reflectance distribution at 532 nm over Antarctica for clear sky (solid curves) and cloud sky conditions (dash curves). The solid red is reflectance directly from the saturated signals. The solid black is reflectance estimated from surface tail with the constant total-to-tail signal ratio of 19.6. The dash red and black are surface reflectance before and after correcting the cloud transmittance. The pink is MODIS reflectance distribution at 555 nm.

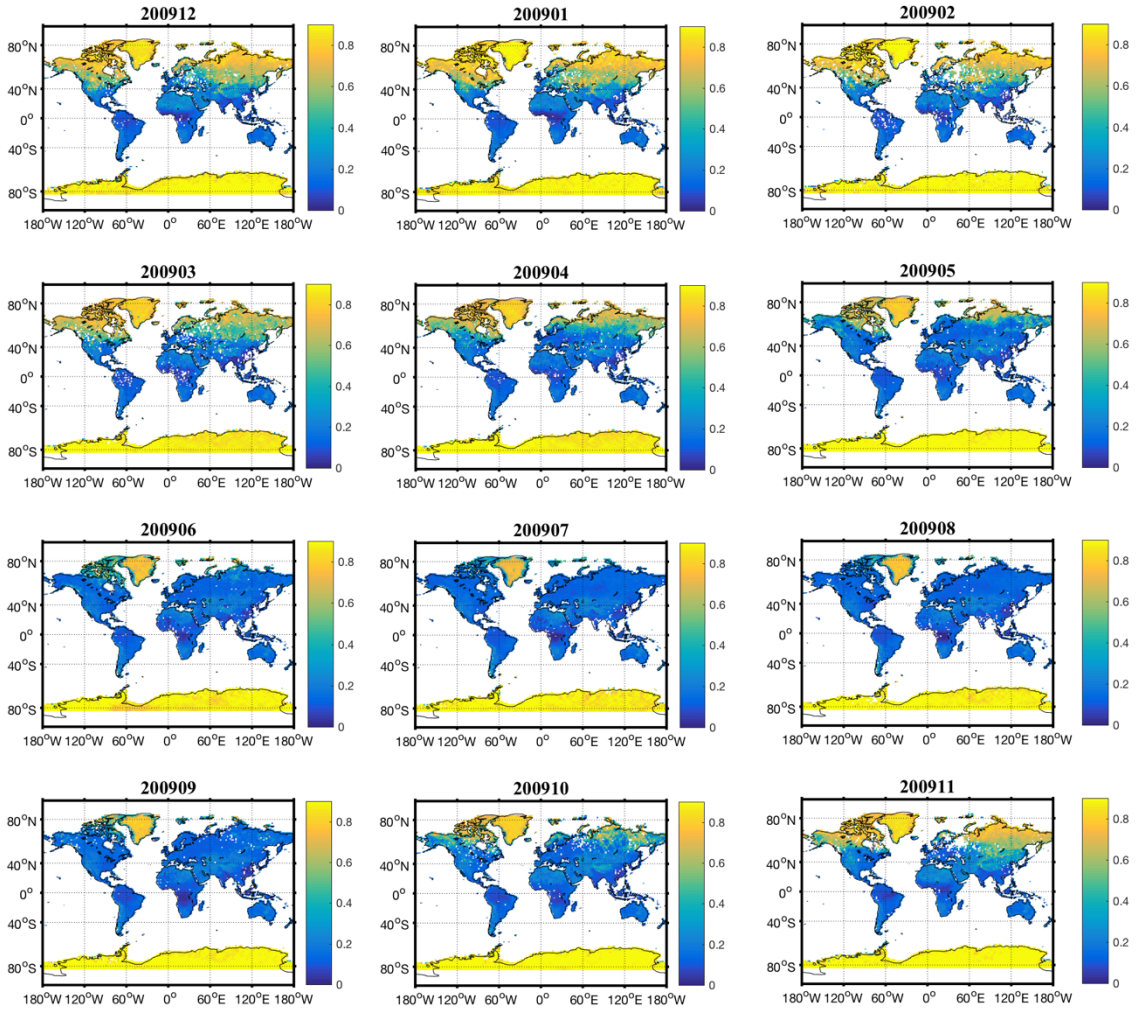

Figure 10 The monthly CALIOP surface reflectance at 532 nm for clear sky condition in 2009. The color bar stands for the value of surface reflectance.

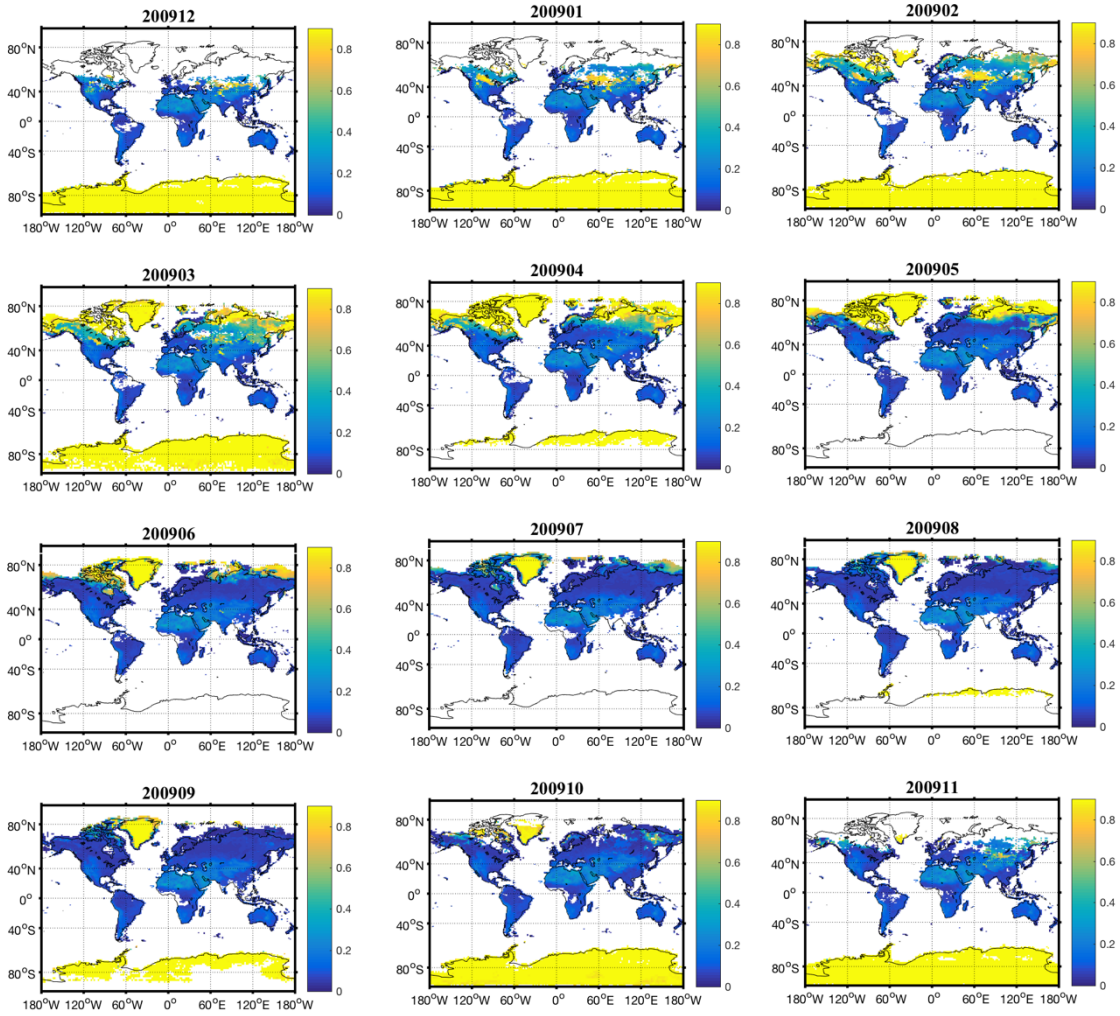

Figure 11 The monthly MODIS surface reflectance at 555 nm in 2009. The color bar stands for the value of surface reflectance. There are no MODIS observations during polar night at high latitudes

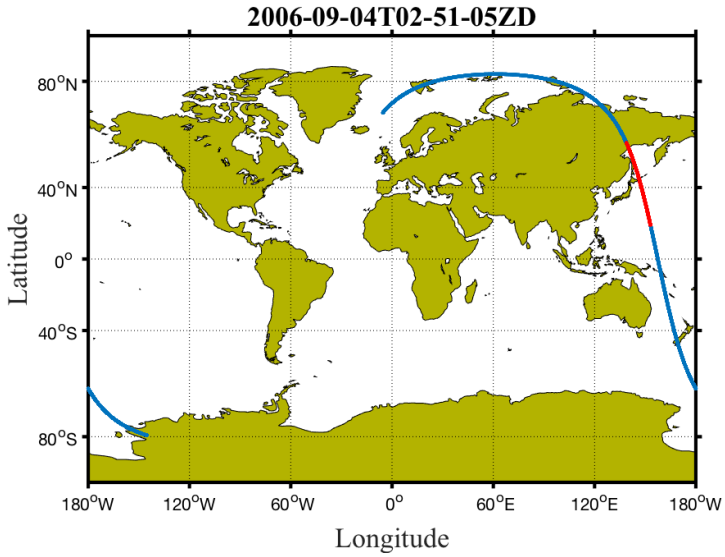

Figure 12 CALIOP ground orbit track. The blue line is the orbit track of one granule around 2:51am on September 4th 2006. The red line is the study region shown in Figure 12 and 13.

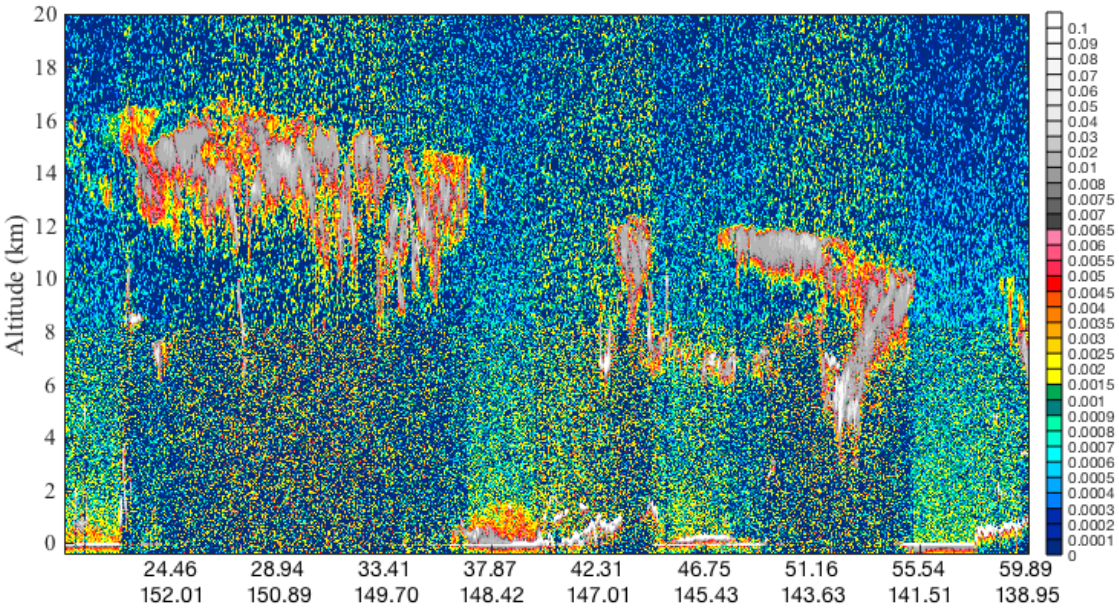

Figure 13 Total attenuated backscatter (/km/sr) along the red line orbit shown in Figure 11. The color bar on the right stands for the value of total attenuated backscatter.

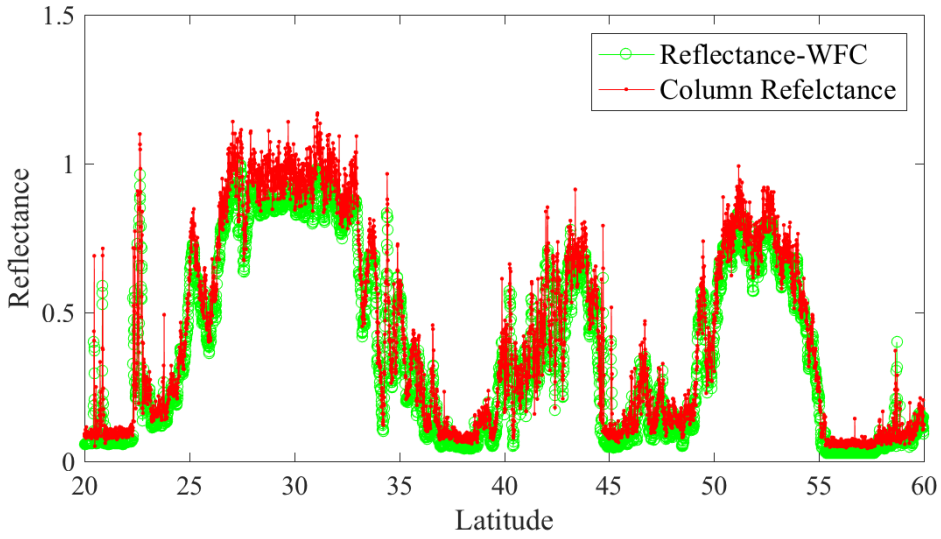

Figure 14. CALIOP Column reflectance (red) compared with the WFC bi-directional reflectance (green).

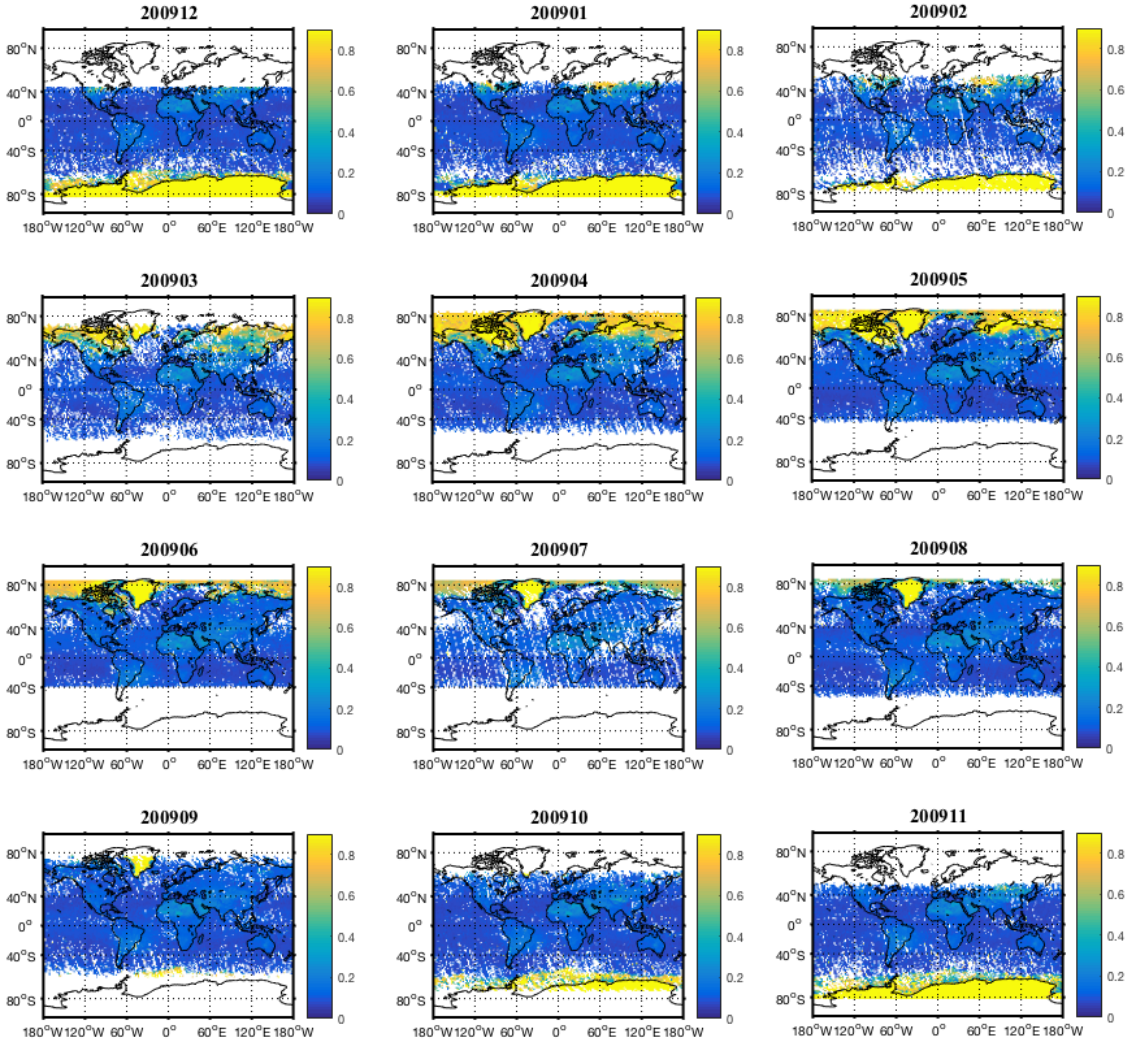

Figure 15. The monthly CALIOP Column reflectance for clear sky condition in 2009. The areas of white are where there are insufficient observations to derive a meaningful value.

5